TiO_2/Au/TiO_2 multilayer thin-film photoanodes synthesized by pulsed laser deposition for photoelectrochemical degradation of organic pollutants

Isidoro Olvera-Rodríguez[a], Rafael Hernández[a], Alejandro Medel[b], Carlos Guzmán[a], Luis Escobar-Alarcón[c], Enric Brillas[d], Ignasi Sirés[d],*, Karen Esquivel[a],**

[a] Posgrado de Ingeniería, Facultad de Ingeniería, Universidad Autónoma de Querétaro, Cerro de las Campanas, C.P. 76000, Santiago de Querétaro, Qro., Mexico

[b] Centro de Investigaciones y Desarrollo Tecnológico en Electroquímica, Parque Tecnológico Querétaro s/n, Sanfandila, Pedro Escobedo, C.P. 76730, Qro., Mexico

[c] Departamento de Física, Instituto Nacional de Investigaciones Nucleares, Carretera México – Toluca s/n, La Marquesa Ocoyoacac, Mexico

[d] Laboratori d'Electroquímica dels Materials i del Medi Ambient, Departament de Química Física, Facultat de Química, Universitat de Barcelona, Martí i Franquès 1-11, 08028 Barcelona, Spain

Paper submitted to be published in *Separation and Purification Technology*

* Corresponding author:	E-mail address: i.sires@ub.edu (I. Sirés)
	Phone: +34 934039240. Fax: +34 934021231
** Corresponding author:	E-mail address: karen.esquivel@uaq.mx (K. Esquivel)
	Phone: +52 (442)192 12 00. Fax: +52 (442) 192 13 25

Abstract

Most commonly employed anodes for photoelectrochemical degradation of organic contaminants in water are too thick, resulting in a lower degradation efficiency due to an excessive electron-hole recombination. Multilayer-type TiO_2/Au/TiO_2 nanocomposites have been prepared as photoanode thin films by pulsed laser deposition (PLD). The films were composed of six TiO_2 and five Au alternate layers, with total thickness of about 212 nm, aimed to optimize the absorption of photons and minimize the recombination. The influence of gold on the optical, structural, and chemical properties of the semiconductor nanocomposites was investigated. The band gap determined from Tauc model was 3.22 eV, close to that obtained by spectroscopic ellipsometry and lower than that of the TiO_2 film, revealing an enhancement of visible light absorption. The catalytic performance of PLD films was evaluated by using them as anodes in electro-oxidation (EO) and photoanodes in photoelectrocatalysis (PEC) to degrade 39-157 mg L^{-1} paracetamol in sulfate medium. The drug removal was very slow in EO, due to the low ability to form $^{\bullet}OH$ on the anode surface, which was significantly enhanced upon UVA irradiation in PEC. The presence of Cl^- allowed a faster degradation by produced active chlorine. Finally, a hybrid process involving PEC + photoelectro-Fenton (PEF) with an air-diffusion cathode yielded total paracetamol decay in 4-5 min at an anodic potential of +4.0 V because of the efficient $^{\bullet}OH$ generation from Fenton's and photo-Fenton reactions. Hydroquinone, *p*-benzoquinone and hydroxylated products were detected during EO and PEC. The generation of active chlorine was confirmed by identifying a chlorinated derivative, *N*-(4-chloro-2-hydroxyphenyl)acetamide, in PEC + PEF treatment.

Keywords: TiO_2/Au/TiO_2 nanocomposites; Paracetamol; Photoanode; Photoelectrocatalysis; Photoelectro-Fenton

1. Introduction

Photoelectrocatalysis (PEC) has emerged in recent years as a low cost electrochemical advanced oxidation process (EAOP) for the efficient destruction of organic pollutants contained in water. This method combines the action of mild photoirradiation and a small anode potential (E_{bias} or E_{an}) or current (I_{appl}) allowing: (i) the promotion of electrons from the valence band (VB) of the photoanode to its conduction band (CB), generating electron-hole pairs on the catalyst surface (reaction (1)); (ii) the spatial separation of both charge carriers by collection of the transferred electrons at the cathode, thus minimizing their recombination with holes; and (iii) the generation of different reactive oxygen species (ROS) that can degrade the organics, like $O_2^{\bullet-}$, $HO_2^{\bullet}$, H_2O_2, O_3 and $^{\bullet}OH$ [1,2]. Among them, hydroxyl radicals ($^{\bullet}OH$) have the pre-eminent oxidizing role due to their high redox potential (E^0 = 2.8 V|SHE), being mainly formed from water oxidation by holes (reaction (2)) [3] or anodic oxidation at the photoanode (M) surface (reaction (3)) [4-7].

$$\text{Photoanode} + h\nu\ (\geq E_{gap}) \rightarrow e^-_{CB} + h^+_{VB,TiO2} \qquad (1)$$

$$h^+_{VB,TiO2} + H_2O \rightarrow {}^{\bullet}OH + H^+ \qquad (2)$$

$$M + H_2O \rightarrow M({}^{\bullet}OH) + H^+ + e^- \qquad (3)$$

The performance of conventional PEC can be enhanced by employing a cathode with great ability to electrogenerate H_2O_2 from two-electron O_2 reduction. This reaction is especially efficient at carbonaceous substrates such as supported particles [8-11], fibers [12,13], nanotubes [14,15], graphene [16,17], felts [18,19] or air-diffusion materials [20]. H_2O_2 can be reduced to $^{\bullet}OH$ by e^-_{CB} via reaction (4) [21], although there is controversy about the occurrence of such transformation [22]. Alternatively, H_2O_2 can be activated in other EAOPs by metal catalysts like Fe^{2+} to yield $^{\bullet}OH$ via Fenton's reaction (5), giving rise to the electro-Fenton (EF) process [23,24]. The catalytic cycle can be sustained upon irradiation of the solution with UVA light or sunlight in photoelectro-Fenton (PEF) and solar photoelectro-Fenton (SPEF) systems, which allow the Fe^{3+} photoreduction to Fe^{2+} as well as the gradual photodegradation of refractory metalorganic complexes [20,25]. It is worth to notice that few works have investigated the coupling between PEC and EF [26,27] or PEF [21].

$$e^{-}_{CB} + H_2O_2 \rightarrow {}^{\bullet}OH + OH^{-} \quad (4)$$

$$Fe^{2+} + H_2O_2 \rightarrow Fe^{3+} + {}^{\bullet}OH + OH^{-} \quad (5)$$

TiO_2 in its crystalline anatase phase is the most widely employed catalyst for photoelectrochemical water decontamination, owing to its many virtues like non-toxicity, low cost, excellent chemical and photochemical stability, and moderate band gap near the visible range (3.2 eV, λ = 387.5 nm) [1]. In general, it is employed either as a nanostructure or a thin film. In particular, there exist several deposition methods to grow high quality thin films. The sol-gel synthesis is very common, but other techniques like particle assembly (e.g., electrophoresis), aqueous phase deposition (e.g., anodization, electrodeposition, and thermal decomposition) and gas phase deposition (e.g., chemical vapor deposition, magnetron sputtering, and spray coating) have also been investigated [28]. A less explored method is pulsed laser deposition (PLD), which relies on substrate-coating by laser-induced plasma [29]. Its advantages include flexibility, quick response, and congruent evaporation, yielding highly crystalline and stoichiometric deposits [30].

The modification of TiO_2 with transition metals such as Cr, Co, or Fe allows extending the TiO_2 absorption into the visible region but, in turn, they act as sites that stimulate the electron-hole pair recombination and thermal instability [31]. Better performance of TiO_2-based heterostructures results from decoration with Cu [32-34] or noble metals like Ag [35,36], Pd [37] and Au [38] due to their different Fermi level as compared to TiO_2. Noble metals act as an additional electron sink, facilitating the electron transfer from the semiconductor CB to the metal particle. This improves the quantum yield because the electron-hole recombination is reduced. Furthermore, these metals allow harnessing the surface-plasmon resonance effect under visible light irradiation [39]. In the case of Au-TiO_2 nanocomposites, visible light at $\lambda = 560$ nm (close to the surface plasmon resonance [40]) may excite electrons from Au nanoparticles, to be further transferred to the CB of TiO_2. Consequently, the accumulation of charge carriers is increased. In addition, as shown in reaction (6), $^{\bullet}OH$ may be formed on the Au surface upon oxidation of water [41]. The potential occurrence of Au^+ and Au^{3+} species also serves for the separation charge carriers [1].

$$h^+_{VB,Au} + H_2O \rightarrow {}^{\bullet}OH + H^+ \qquad (6)$$

Some authors have prepared Au-TiO_2 nanocomposite thin films as photoanodes by PLD method, because of their precise and simultaneous control of stoichiometry, crystallinity and thickness of the growing films upon accurate selection of the experimental process parameters [42,43]. Several multilayer electrodes composed of Ni-Cu and Zn-Ni have been proven to improve the mechanical and corrosive properties, reaching a higher catalytic activity with longer service life as compared to simple alloys [44,45]. However, to the best of our knowledge, the preparation of Au-TiO_2 multilayer electrodes and their application as photoanodes for organic pollutants degradation has not been reported so far.

At present, many freshwater resources are seriously jeopardized by the presence of all classes of pharmaceuticals used in human and veterinary medicine, which potentially entail serious threats. The high relevance of this topic is confirmed from recent thematic surveys conducted by world organizations like UNESCO [46], which have revealed the presence of paracetamol (*N*-(4-hydroxyphenyl)acetamide) in the Baltic Sea. Worth highlighting, paracetamol was the most prescribed drug in 2017 [47]. Several authors have treated pharmaceuticals in aqueous media by PEC with TiO_2-based photoanodes [3,48-51], whereas decoration with noble metals has been rarely addressed. For example, acetylsalicylic acid was totally degraded by PEC with Pt-TiO_2 [52] and Pd-TiO_2 [53] under Xenon light illumination.

This work reports the synthesis of thin-film sandwich-type composites of TiO_2/Au/TiO_2 by PLD, aiming to enhance the photon adsorption and minimize the electron-hole pair recombination upon PEC. The morphological, structural, and optical properties of synthesized materials were analyzed by scanning electron microscopy (SEM), energy dispersive X-ray spectroscopy (EDS), X-ray photoelectron spectroscopy (XPS), Raman spectroscopy, elastic forward analysis (EFA), UV/Vis spectroscopy, photoluminescence, and spectroscopic ellipsometry, whereas electrochemical characterization was made by cyclic voltammetry. The PEC treatment of paracetamol solutions in sulfate medium in the absence and presence of chloride ion was investigated for the best TiO_2/Au/TiO_2 film as photoanode. The hybrid degradation by PEC + PEF was also examined.

2. Experimental

2.1. Chemicals

Paracetamol (99.9%) was of reagent grade purchased from Merck and used as received. Sulfuric acid (used to adjust the pH), anhydrous sodium sulfate and sodium chloride (background electrolytes) and Fe(II) sulfate heptahydrate (catalyst source for Fenton's reaction) were of analytical grade purchased from Fluka and Panreac. All solutions were prepared with pure water (Millipore Milli–Q system, resistivity >18.2 MΩ cm at room temperature). Other chemicals were also of reagent or HPLC grade purchased from Sigma-Aldrich, Probus and Panreac.

2.2. Synthesis of thin-film photoanodes

Different deposition conditions were employed in order to optimize the properties and performance of the thin films obtained by PLD. Hereby, the optimum parameters are described. Once the pressure, close to 8×10^{-6} Torr, was reached in the reaction chamber, the deposition was performed. Multilayer thin films were deposited by alternating two laser ablation plasmas produced using an Nd:YAG laser, with emission at the third harmonic (λ = 355 nm) and a pulse duration of 5 ns, working at a frequency of 10 Hz. For this purpose, the laser beam was divided in two using a beam splitter. The obtained laser beams were focused onto the targets with 50 cm focal length spherical lenses. High purity (99.99%) TiO_2 and gold were used as targets. The laser fluence on both targets was constant, close to 4.0 J cm^{-2}. The multilayer structure was obtained as follows: (i) the deposition started with only the TiO_2 ablation plasma acting for 5 min; (ii) afterwards, the laser beam on the TiO_2 target was blocked using a mechanical shutter and the gold ablation plasma was produced for 30 s; (iii) the laser beam on the Au target was then blocked and the ablation of the TiO_2 target was initiated again. This procedure was repeated 5 times to attain a deposition time of 2.5 min for Au. The film was deposited on a conductive glass substrate of 4.5 cm^2 surface area placed at 7 cm from the TiO_2 target surface.

2.3. Procedures and characterization techniques

The gold content in the films was determined by EDS using a microprobe attached to a JEOL JSM 6510LV scanning electron microscope, with an acceleration voltage of 15 kV. XPS was used to determine the chemical states of the elements in the films. The measurements were performed in a PHI 5500 Multitechnique System from Physical Electronics, with a monochromatic X-ray source (aluminum Kα line of 1486.6 eV and 350 W) placed perpendicular to the analyzer axis and calibrated using the $3d_{5/2}$ line of Ag with a full width at half maximum (FWHM) of 0.8 eV. The analyzed area was a circle of 0.8 mm diameter, whereas the selected resolution for the spectra was 187.85 eV of Pass Energy (PE) and 0.8 eV per step for the survey spectra and PE = 23.5 eV and 0.1 eV per step for the narrow spectra of the different elements. All measurements were made in an ultra-high vacuum (UHV) chamber at pressures between 5×10^{-9} and 2×10^{-8} Torr. The EFA characterization was carried out using a 12.0 MeV C^{2+} ion beam from a Tandem Van de Graff accelerator. The angle between the ion beam and the sample surface was set at 30° while the angle between the detected particles and the incident ion beam was 45°. The microstructure was studied by Raman spectroscopy, employing a micro-Raman LabRam 800 system equipped with a confocal Olympus BX40 microscope and a 100X objective. The energy source was an Nd:YAG laser at the second harmonic (λ = 532 nm) and the spectra were calibrated with the monocrystalline Si line at 521 cm^{-1}.

Optical measurements were performed on a Perkin Elmer Lambda 35 UV/Vis spectrophotometer to obtain the transmittance spectra of the films from 200 to 800 nm. A FluoroMax 4 spectrofluorometer from Horiba Jobin Yvon was used to obtain the photoluminescence (PL) spectra employing a 150 W Xenon lamp as excitation source. Emission spectra were acquired from 365 to 650 nm, in order to avoid the first and second order of the Rayleigh scattering, using 350 nm excitation wavelength.

The spectroscopic ellipsometry was performed in a M44 J.A Woollam rotating analyzer ellipsometer, with an incidence angle of 70°. The ellipsometric parameters (amplitude psi, and phase delta) were measured in the 1.62-4.40 eV photon energy range (763.2-281.5 nm). The method used to analyze the results was effective medium approximation (EMA) model in order to obtain the optical properties of the deposits.

The electrochemical characterization was performed by cyclic voltammetry with an Autolab PGSTAT30 potentiostat. Up to 5 consecutive cycles were made at 100 mV s^{-1} within the range from +3 V to -2 V vs. Ag|AgCl. An undivided electrochemical cell containing 50 mL of 0.050 M Na_2SO_4 at pH 3.0 thermostated at 25 ºC was used. It was equipped with a synthesized thin-film nanocomposite, a rolled platinum thread, and Ag|AgCl (3 M KCl) electrode as the working, counter, and auxiliary electrodes, respectively. The exposed area of the working electrode was 1 cm^2. All potentials are referred to the reference electrode. Before each run, O_2 was purged from the solution with gentle N_2 stream for 20 min, keeping it above the solution during the analysis. Comparative cyclic voltammograms were made with pure gold and undoped thin film as the anode to better characterize the behavior of the $TiO_2/Au/TiO_2$ films.

The pH and electrical conductance of all solutions were measured with a Crison 2000 pH-meter and a Metrohm 644 conductometer, respectively. To assess the paracetamol degradation, samples of 1.5 mL were withdrawn every 30 or 60 min, immediately diluted with acetonitrile to stop the degradation and then, 50 μL aliquots were injected into a Waters 600 LC fitted with a C18 BDS Hypersil, 250 mm × 4.6 mm, column with particle size of 5 µm. Isocratic analyses were carried out using a 70:30 (v/v) acetonitrile/K_2HPO_4 mixture as mobile phase at 0.8 mL min^{-1}. The retention time for paracetamol was 2.5 min, showing a characteristic absorption peak at $\lambda = 243$ nm. All samples were microfiltered with 0.45 µm Whatman PTFE filters. Experiments were run at least in duplicate and mean values from HPLC analyses are reported.

GC-MS analysis of treated solutions was made with an Agilent Technologies system composed of a 6890N gas chromatograph coupled to a 5975C mass spectrometer in EI mode at 70 eV. A nonpolar Teknokroma Sapiens-X5ms and a polar HP INNOWax column, both of 0.25 µm, 30 m × 0.25 mm, were used. The temperature ramp was: 36 ºC for 1 min, 5 ºC min^{-1} up to 320 ºC, and hold time of 10 min. The temperatures of the inlet, source and transfer line were 250, 230 and 300 ºC, respectively. Liquid-liquid extractions were employed to obtain the final samples to be injected. The mass spectra were analyzed with NIST05 MS database.

2.4. Treatment of paracetamol solutions

To evaluate the electroactivity and photoactivity of the synthesized thin films, paracetamol was used as model pollutant. An open, undivided electrochemical cell, thermostated at room temperature and containing 100 mL of solution, was employed. A multilayer film anode was combined with a 316L stainless steel plate cathode, placed at a distance of 2.5 cm and both with a geometric area of 4.3 cm^2. Paracetamol solutions (39-157 mg L^{-1}) in 0.050 M Na_2SO_4 or 0.035 M Na_2SO_4 + 0.015 M NaCl mixtures with the same conductivity were treated at pH 3.0 and room temperature by electrochemical oxidation (EO, without UVA radiation) and PEC using an Amel 2049 potentiostat-galvanostat, whereas the potential difference between the anode and cathode (E_{cell}) was measured on a Demestres 601BR digital multimeter. These experiments were carried out in galvanostatic mode, and the effect of the I_{appl} value was studied in PEC by running tests at 0.50, 1.00 and 1.50 mA (E_{an} of 1.7, 2.2 and 2.8 V vs. Ag|AgCl, and E_{cell} of 1.9, 2.7 and 3.3 V, respectively). From this study and aiming to ensure the largest stability of the photoanode, 0.50 mA was selected as optimum I_{appl}. In all cases, the solution was magnetically stirred at 800 rpm and the experiments lasted 360 min. For the photo-assisted tests, a 36 W semicircular LED UVA lamp surrounding the cell was used as the light source, and the entire setup was placed in a purpose-made mirror box to favor the radiation collection through the solution. The UV irradiance was 88 W m^{-2}, as measured on a radiometer.

In the PEC + PEF experiments, the stainless steel plate was replaced by a 3 cm^2 carbon-polytetrafluoroethylene air-diffusion cathode supplied by Sainergy Fuel Cell, mounted as described elsewhere and fed with air pumped at 1 L min^{-1} for continuous H_2O_2 generation [54,55]. A concentration of 0.50 mM Fe_2SO_4 was employed and the interelectrode gap was about 1 cm. The applied E_{an} was +4.0 V vs. Ag|AgCl, yielding E_{cell} = 4.6 V. In all cases, the solution pH was chosen as 3.0 since it is the optimum value for Fenton's reaction (5) occurring in PEF.

3. Results and discussion

3.1. Characterization of thin films

The photoelectrochemical activity of TiO_2-based films depends on their morphological, structural, optical, and electrical properties. In particular, it is crucial to keep the thickness of the deposit as low as possible, being the thin films the most efficient alternatives. Thick coatings lead to the presence of useless material, which cannot be photoactivated and, in addition, increases the recombination.

Semi-transparent TiO_2/Au/TiO_2 thin films were obtained at the optimum deposition conditions described in Section 2.1. According to SEM analysis (not shown), the surface was smooth with some dispersed gold nanoparticles with diameter around 25 nm. The corresponding EDS analysis allowed determining the composition of the thin film as 87.8 at.% oxygen, 11.8 at.% titanium, and 0.4 at.% gold.

The XPS spectrum of Fig. 1 evidences the presence of signals related to oxygen, titanium and gold in the thin film. The other signals correspond to the substrate (Si 1s) and to adventitious carbon. The signals at 460, 59 and 33 eV can be related to different orbital line positions of titanium. The signal at 530 eV is ascribed to oxygen (O 1s), whereas that at 87 eV belongs to gold (Au 4f). Fig. S1 in Supplementary Material shows the XPS spectrum of each element. The Ti 2p region shown in Fig. S1-A reveals the presence of two signals: the first one located at 457.9 eV and the second one at 463.5 eV, corresponding to the $2p_{3/2}$ and $2p_{1/2}$ orbital levels, due to the spin orbital coupling effect, which can be attributed to Ti^{4+} [56-59], with binding energy difference of 5.6 eV [60]. Note that a mathematical analysis of the Ti 2p region showed that the Ti^{4+} and Ti^{3+} signals appeared in the same position, suggesting that both oxidation states of the titanium are actually present in the composite. The XPS spectrum of gold in Fig. S1-B presents two main signals, thus forming a doublet: one at 84.3 eV corresponding to Au $4f_{7/2}$ core level and another peak at 89.4 eV corresponding to Au $4f_{5/2}$. The XPS spectrum of O 1s in Fig. S1-C suggests that the lattice of the material was modified. This is inferred from the band located at about 530 eV, which is composed of three signals:

the first one at 529.0 eV attributed to the oxygen vacancies, the next peak at 530.7 eV due to the ordering in the lattice of Ti-O-Ti (i.e., crystal lattice oxygen), and the last one at 531.9 eV arising from the formation of hydroxyl groups on the TiO_2 surface [61]. The oxygen vacancies were formed by the presence of gold in the structure [61,62]. The XPS spectrum of C 1s in Fig. S1-D shows three signals: the band at 284.0 eV corresponds to the C-C bond, and other one, at 287.8 eV, can be explained by the interaction between carbon and oxygen in the surface [56,58,63].

The Raman spectrum shown in Fig. 2 displays vibrational modes at 139 cm^{-1} (B_{1g}), 445 cm^{-1} (E_g), 607 cm^{-1} (A_{1g}), and 795 cm^{-1} (B_{2g}) corresponding to the rutile crystalline phase of TiO_2 [59,64]. A shift of the B_{1g} signal, from 145 to 139 cm^{-1}, is observed, suggesting distortion of the TiO_2 lattice due to the presence of gold. The features of the Raman spectrum indicate high crystallinity of the thin film. Furthermore, regarding the vibrational modes, the lattice vibrations could be assigned as follows: (i) the B_{1g} mode corresponds to a symmetric bending vibration of O-Ti-O, (ii) the E_g mode is due to a symmetric stretching vibration of O-Ti-O, and (iii) the A_{1g} mode is attributed to an anti-symmetric bending vibration of O-Ti-O. Considering the main vibrational modes E_g and A_{1g}, it is possible to determine the role of the phonons in the excitation process of the lattice. The first one (E_g) is produced by acoustic phonons that could contribute to the promotion of charge separation, whereas the second one is caused by longitudinal optical phonons that promoted a higher recombination time and, simultaneously, the generation of superoxide radicals since they are located in the conduction band [65].

To gain better insight about gold distribution in the film, EFA analysis was carried out. The general spectrum of Fig. 3A shows the signals of the elements present in the film, namely O, Si, Ti and Au, in good agreement with the chemical composition determined by EDS. The Si signal was due to the substrate. Fig. 3B shows the signal corresponding to Ti, revealing that this element is distributed almost uniformly along the film thickness, with a slight increase in the interface direction. Fig. 3C shows five well-defined peaks arising from the five gold layers sandwiched by titania, thus forming the thin film structure (TiO_2/Au/TiO_2/Au/TiO_2/Au/TiO_2/Au/TiO_2/Au/TiO_2) [66,67]. Note that equidistant peaks are indicative of good control in the location of Au within the multilayer structure upon variation of Ti deposition time. The Au signals increase from the inner to the outlet layer, in agreement with the decrease of the Ti signal. Therefore, EFA results provide a clear evidence of the multilayer structure formed.

The transmittance spectra of Fig. 4A show that the addition of gold in the film has two important effects: it improves the light absorption and shifts the absorption edge to the visible spectral region, which was one of the goals of this work. Another obvious feature in the transmittance spectra is the presence of maxima and minima, which are due to interference effects [68], from which the thickness and refractive index can be determined using the model of Goodman [69]. The thickness values were 188 nm for the sample without gold and 212 nm for the one containing gold. For the same samples, the refractive index was 2.4 and to 2.1, respectively. In addition, the band gap was determined from the UV/Vis spectra using the Tauc method assuming indirect transitions [70]. This was done by plotting $(\alpha h\nu)^2$ as a function of the energy, as depicted in Fig. 4B. The optical absorption coefficient was obtained as $\alpha = -\ln(T)/t$, where t is the film thickness and T the transmittance. Fig. 4B shows the linear fits and the band gap value obtained for each film. Good fits to the experimental curves were obtained for both samples. As can be seen, the band gap value obtained for the TiO_2 film was 3.48 eV, whereas a lower value, 3.22 eV, was obtained for the multilayer film [61]. The higher band gap of undoped TiO_2 as compared to typical TiO_2 can be attributed to the presence of oxygen vacancies, which act as barriers and hence, the whole composite behaves as a kind of electrical insulator. Consequently, the photon effect over the surface causes a shift of the band gap, requiring a higher energy to be activated.

Fig. 5A shows that the PL spectrum of the TiO_2 film consists of a broad emission band from 2.0 to 3.3 eV, which can be mainly attributed to oxygen vacancies. The maximum of emission found at 3.09 eV can be related to an interband transition. The high intensity of the PL signal suggests a high recombination rate of the photogenerated charges in this sample. When gold was incorporated in the film, a strong quenching of PL emission (Fig. 5A) as well as a red shift (Fig. 5B) were observed. These results reveal that PL emission depends strongly on the Au presence, promoting a decrease of the recombination rate. This result suggests a more suitable photocatalytic response of the TiO_2/Au/TiO_2 multilayer thin film.

To confirm the results obtained by UV/Vis and PL spectroscopy, spectroscopic ellipsometry analysis was carried out. To reproduce the parameters, a stratified model was required, which could be simple as an interface or very complex. Based on the morphology of the films, the properties of a mixture of two materials, Au and TiO_2, were simulated to emulate an effective refractive index of the layer using the EMA model, which allows approximating the optical properties of the whole thin film and addresses the individual properties of the material and its volume fraction contribution. The model was adjusted until a suitable agreement between the experimental values and the model of psi (Ψ) and delta (Δ) fitted values vs the wavelength was obtained [71]. The good fit shown in Fig. S2 in Supplementary Material allowed determining a roughness value of 13.75 ± 2.22 nm, practically invariable in all the film. This is a good feature because it means that the surface will be hard to mess up by the penetration of the dissolved pollutants when it will be used in the photocatalytic tests.

The band gap value was alternatively obtained from ellipsometric measurements by plotting the absorption coefficient vs energy. Since the Au/TiO_2/Au multilayer thin film exhibited a certain thickness gradient, up to three different colored fringes (yellow, blue, and purple) were observed on its surface. Hence, three curves were obtained, one for each zone in the film, which were compared with a titanium blank, as can be seen in Fig. S3 in Supplementary Material. In the three scanned zones, the band gap value showed almost no variation and thus, it is possible to state that the excitation energy was not influenced by the changing films thickness. Furthermore, it can be observed that the band gap changed when the material was modified with gold, also changing the optical constant, which again confirms the enhanced light absorption as a result of the presence of oxygen vacancies [42]. Worth noting, the band gap values were near to those obtained from Tauc plots (Fig. 4B).

From EFA and ellipsometry spectroscopy, it is clear that gold was distributed with a gradient over the surface. This does not imply a variation in the optical parameters along the thin film, which remained constant, but it is evident that the gold incorporation in the titania changed the optical response of the material, with dominance of the TiO_2 optical properties in the thin film. This suggests that even performing the synthesis of independent layers, gold mainly behave as a dopant that improved the optical performance of TiO_2.

3.2. Electrochemical activity of thin films

The electrochemical behavior of the synthesized multilayer thin film was studied by cyclic voltammetry in 0.050 M Na_2SO_4 at pH 3.0. Fig. 6A and B present the cyclic voltammograms recorded for pure Au and the unmodified TiO_2 film, respectively, under the same conditions at a scan rate of 100 mV s^{-1}. Fig. 6A shows the expected *I-E* plot for pure Au within the potential window from -0.80 to +1.25 V, with the oxidation peak of Au to Au_2O_3 close to +0.74 V and the corresponding reduction peak at +0.46 V, in agreement with previous work [72]. In the case of TiO_2, Fig. 6B evidences a clear oxidation of water originating adsorbed $^{\bullet}OH$ within the potential range between +0.50 and -2.00 V [73]. On the other hand, Fig. 6C depicts the profile obtained for the TiO_2/Au/TiO_2 multilayer anode, where a shift to more positive values of the oxidation/reduction peaks potentials related to Au, as well as the adsorption/desorption potentials for $^{\bullet}OH$ corresponding to TiO_2 can be observed. This can be attributed to superficial defects of the anode. These findings suggest that pollutants could be oxidized more rapidly, thus enhancing the removal efficiency. Note that the potential window for the multilayer film was narrowed as compared to that of the unmodified one (see Fig. 6B and C), which may be an effect of the superficial defects promoted by the gold incorporation in the lattice.

An electrochemical surface area of 0.9912 cm^2 with a roughness factor of 0.2305 was estimated for the multilayer thin film using the desorption hydrogen zone between +0.02 and -0.29 V. This area is close to the geometric one of 1 cm^2 considered for the cyclic voltammetry experiments. Since the thickness of the film was very small, around 212 nm, one can infer that the electrode surface possessed a low active site density.

3.3. Paracetamol degradation by single and hybrid PEC processes

The performance of the multilayer thin film as anode or photoanode was assessed from the degradation of 100 mL of aqueous solutions of paracetamol at pH 3.0. Several preliminary tests were made with 157 mg L^{-1} of the drug: (i) no change in its concentration was found by direct irradiation of the solution with the 36-W LED UVA lamp, suggesting that paracetamol was not photoactive under such conditions, (ii) a very small drug decay was obtained upon irradiation of a $TiO_2/Au/TiO_2$ thin film of 4.3 cm^2 area immersed in the solution, evidencing the accumulation of a low quantity of $^{\bullet}OH$ from reactions (2) and (6) by photocatalysis, due to the fast electron-hole recombination, and (iii) similar degradation performances were measured by applying 0.50, 1.00, and 1.50 mA under PEC conditions and hence, to ensure the highest stability and duration of the film, an I_{app} = 0.50 mA was utilized in galvanostatic PEC experiments.

Several assays were made to show the performance of PEC for paracetamol contents between 39 and 157 mg L^{-1} in sulfate matrices without or with Cl^{-}. First, comparative EO experiments were made in 0.050 M Na_2SO_4 and the results are presented in Fig. 7A. As can be seen, a gradual normalized drug decay was always found until 300 min of treatment, attaining a smaller reduction of 47%, 37%, and 29% as the drug content was increased. Since at I_{app} = 0.50 mA the E_{an} was +1.7 V, higher than the potential value needed for water oxidation to $^{\bullet}OH$ via reaction (3), one can expect a certain production of this radical with ability to attack the drug, in concomitance with its direct anodic oxidation. Note that, in these trials, the total content of paracetamol degraded gradually rose. The quantity of available $^{\bullet}OH$ was enhanced due to the deceleration of the parasitic reactions of this radical, pre-eminently its oxidation to O_2 [4,23,24]. The same reasons can justify the greater drug content removed, although accounting for a lower percentage, at higher organic load upon PEC treatment in 0.050 M Na_2SO_4 (Fig. 7B). In this case, the large quantity of additional $^{\bullet}OH$ formed from reactions (2) and (6) under UVA light irradiation, resulting from the minimization of the electron-pair recombination thanks to current supply, caused a faster degradation as compared to EO. Thus, 95%, 69% and 61% drug disappeared at the end of the treatment of 39, 78 and 157 mg L^{-1} paracetamol, respectively. The pollutant decayed much more rapidly in a mixed sulfate + chloride matrix (Fig. 7C), yielding overall removal at 120 min for 39 mg L^{-1} and at 150 min for 78 mg L^{-1}, but only attaining a 50% decay for 157 mg L^{-1}. The faster degradation in the two former solutions can be ascribed to the quicker destruction of organics by active chlorine species formed from oxidation of Cl^{-} to dissolved Cl_2 at the photoanode via reaction (7), followed by hydrolysis to hypochlorous acid (HClO) via reaction (8) [74]. HClO is the strongest active chlorine species and predominates over Cl_2 at pH 3.0, then competing with $^{\bullet}OH$ to attack the paracetamol molecules [8,23,24]. However, it is well known that $^{\bullet}OH$ may be scavenged by Cl^{-}. The partial destruction of generated radicals could explain the strong inhibition of drug decay in Fig. 7C at 157 mg L^{-1}, suggesting that the oxidation of paracetamol at low concentrations is pre-eminently determined by $^{\bullet}OH$.

$$2Cl^{-} \rightarrow Cl_{2(aq)} + 2e^{-} \quad (7)$$

$$Cl_{2(aq)} + H_2O \rightarrow HClO + Cl^{-} + H^{+} \quad (8)$$

Finally, the performance of the hybrid PEC + PEF process to degrade 39 mg L^{-1} of paracetamol in the mixed matrix with 0.50 mM Fe^{2+} using an air-diffusion cathode for H_2O_2 production was assessed. Fig. 8 evidences a total drug removal after only 4-5 min of treatment, a time much shorter than by single PEC (Fig. 7C). This result can be explained by the fast destruction of the parent molecule with the high amounts of $^{\bullet}OH$ formed from Fenton's reaction (5) in the bulk, much superior to the action of the other oxidizing agents formed at the photoanode. In PEF treatment of 157 mg L^{-1} paracetamol in 0.050 M Na_2SO_4 with 1 mM Fe^{2+} at pH 3.0 using a similar Pt/air-diffusion cell and working at 300 mA (i.e., E_{cell} of 13.0 V), a time of 6 min was needed for the total abatement of the drug [75]. The PEC + PEF treatment with the TiO_2/Au/TiO_2 photoanode showed a greater viability, not only by the shorter time needed for paracetamol disappearance, but also by the use of a less expensive anode and the smaller energy consumption. E_{cell} was as low as 4.6 V at E_{an} = +4.0 V (i.e,, current of 2.00 mA), making the process more cost-effective.

GC-MS analysis of the 39 mg L^{-1} paracetamol solution in 0.050 M Na_2SO_4 treated by EO and PEC showed the formation of aromatic products such as hydroquinone, its oxidation product *p*-benzoquinone and hydroxylated derivatives like tetrahydroxy-*p*-benzoquinone. Hydroquinone can be produced from the attack of $^{\bullet}OH$ on the C(1)-position of the benzenic ring of paracetamol with loss of acetamide [75]. These products have also been reported for the treatment of this drug by several EAOPs [75-77]. The GC-MS analysis of the treated paracetamol solution in the mixed matrix by the hybrid PEC + PEF process also allowed the detection of a chlorinated product, namely *N*-(4-chloro-2-hydroxyphenyl)acetamide, during the first 30 min of electrolysis, whereupon chlorinated molecules were no longer found. The existence of this chlorinated product confirms the production of active chlorine that attacks the C(4)-position of the target molecule, along with its hydroxylation on C(2)-position.

4. Conclusions

A novel TiO_2/Au/TiO_2 multilayer thin-film photoanode was obtained by PLD process, showing a better visible light absorption than TiO_2. According to the optical characterization by UV/Vis spectroscopy, photoluminescence and ellipsometry, the improved photoactivity was due to gold incorporation in the titania matrix. From the structural analysis, rutile was found as main titania phase, whereas the chemical interaction studied by XPS agreed with the presence of metallic gold and Ti^{3+} in the oxide structure. The thin film was employed as anode and photoanode to remove paracetamol from aqueous solutions. The EO treatment of 39 mg L^{-1} of the drug in sulfate medium yielded a low degradation rate, only reaching 47% removal, whereas irradiation with UVA light under the same conditions enhanced the concentration decay up to 95%. The required time was halved upon production of active chlorine in the presence of chloride ion. Finally the hybrid PEC + PEF process exhibited an excellent synergy, achieving the complete disappearance of paracetamol in only 5 min. Hydroquinone, *p*-benzoquinone and hydroxylated products were detected during EO and PEC using 0.050 M Na_2SO_4, whereas a chlorinated derivative was identified during PEC + PEF in the mixed matrix, confirming the generation of active chlorine. The photoactivity of Au-modified TiO_2 thin films within the visible range opens the door to their application in solar PEC and SPEC + SPEF treatments of organic pollutants.

Acknowledgments

The authors gratefully acknowledge financial support from project CTQ2016-78616-R (AEI/FEDER, EU) and project CB-240998 (CONACYT, Mexico). I. Olvera-Rodríguez thanks CONACYT for his fellowship and K. Esquivel thanks funding from FOFI-UAQ-2018 project.

References

[1] H. Zhang, G. Chen, D.W. Bahnemann, Environmental Photo(electro)catalysis: Fundamental Principles and Applied Catalysts; in C. Comninellis, G. Chen (eds.), Electrochemistry for the Environment, Springer Science+Business Media, LLC, New York, USA, 2010.

[2] D. Cao, Y. Wang, X. Zhao, Combination of photocatalytic and electrochemical degradation of organic pollutants from water, Curr. Opinion Green Sustain. Chem. 6 (2017) 78-84.

[3] S. Garcia-Segura, E. Brillas, Applied photoelectrocatalysis on the degradation of organic pollutants in wastewaters, J. Photochem. Photobiol. C: Photochem. Rev. 31 (2017) 1-35.

[4] M. Panizza, G. Cerisola, Direct and mediated anodic oxidation of organic pollutants, Chem. Rev. 109 (2009) 6541-6569.

[5] X. Yu, X. Han, Z. Zhenhuan, J. Zhang, W. Guo, C. Pan, A. Li, H. Liu, Z. Lin, Hierarchical TiO_2 nanowire/graphite fiber photoelectrocatalysis setup powered by a wind-driven nanogenerator: a highly efficient photoelectrocatalytic device entirely based on renewable energy, Nano Energy 11 (2015) 19-27.

[6] G. Avgouropoulos, D. Mantzavinos, P. Lianos, Photoelectrocatalytic vs. photocatalytic degradation of organic water born pollutants, Catalysts 8 (2018) 455 (10 pages).

[7] A. Turolla, M. Bestetti, M. Antonelli, Optimization of heterogeneous photoelectrocatalysis on nanotubular TiO_2 electrodes: reactor configuration and kinetic modelling, Chem. Eng. Sci. 182 (2018) 171-179.

[8] A. Thiam, E. Brillas, F. Centellas, P.L. Cabot, I. Sirés, Electrochemical reactivity of Ponceau 4R (food additive E124) in different electrolytes and batch cells, Electrochim. Acta 173 (2015) 523-533.

[9] G. Coria, I. Sirés, E. Brillas, J.L. Nava, Influence of the anode material on the degradation of naproxen by Fenton-based electrochemical processes, Chem. Eng. J. 304 (2016) 817-825.

[10] A. Galia, S. Lanzalaco, M.A. Sabatino, C. Dispenza, O. Scialdone, I. Sirés, Crosslinking of poly(vinylpyrrolidone) activated by electrogenerated hydroxyl radicals: a first step towards a simple and cheap synthetic route of nanogel vectors, Electrochem. Commun. 62 (2016) 64-68.

[11] A. Thiam, E. Brillas, J.A. Garrido, R.M. Rodríguez, I. Sirés, Routes for the electrochemical degradation of the artificial food azo-colour Ponceau 4R by advanced oxidation processes, Appl. Catal. B: Environ. 180 (2016) 227-236.

[12] H. Lan, W. He, A. Wang, R. Liu, H. Liu, J. Qu, C.P. Huang, An activated carbon fiber cathode for the degradation of glyphosate in aqueous solutions by the electro-Fenton mode: optimal operational conditions and the deposition of iron on cathode on electrode reusability, Water Res. 105 (2016) 575-582.

[13] C. Trellu, N. Oturan, F.K. Keita, C. Fourdrin, Y. Pechaud, M.A. Oturan, Regeneration of activated carbon fiber by the electro-Fenton process, Environ. Sci. Technol. 52 (2018) 7450-7457.

[14] H. Roth, Y. Gendel, P. Buzatu, O. David, M. Wessling, Tubular carbon nanotube-based gas diffusion electrode removes persistent organic pollutants by a cyclic adsorption – electro-Fenton process, J. Hazard. Mater. 307 (2016) 1-6.

[15] C. Ridruejo, F. Alcaide, G. Álvarez, E. Brillas, I. Sirés, On-Site H_2O_2 electrogeneration at a CoS_2-based air-diffusion cathode for the electrochemical degradation of organic pollutants, J. Electroanal. Chem. 808 (2018) 364-371.

[16] T.X.H. Le, M. Bechelany, S. Lacour, N. Oturan, M.A. Oturan, M. Cretin, High removal efficiency of dye pollutants by electro-Fenton process using a graphene based cathode, Carbon 94 (2015) 1003-1011.

[17] E. Mousset, Z. Wang, J. Hammaker, O. Lefebvre, Physico-chemical properties of pristine graphene and its performance as electrode material for electro-Fenton treatment of wastewater, Electrochim. Acta 214 (2016) 217-230.

[18] N. Barhoumi, L. Labiadh, M.A. Oturan, N. Oturan, A. Gadri, S. Ammar, E. Brillas, Electrochemical mineralization of the antibiotic levofloxin by electro-Fenton-pyrite process, Chemosphere 141 (2015) 250-257.

[19] O. Ganzenko, N. Oturan, I. Sirés, D. Huguenot, E.D. van Hullebusch, G. Esposito, M.A. Oturan, Fast and complete removal of the 5-fluorouracil drug from water by electro-Fenton oxidation, Environ. Chem. Lett. 16 (2018) 281-286.

[20] J.R. Steter, E. Brillas, I. Sirés, Solar photoelectro-Fenton treatment of a mixture of parabens spiked into secondary treated wastewater effluent at low input current, Appl. Catal. B: Environ. 224 (2018) 410-418.

[21] L.C. Almeida, B.F. Silva, M.V.B. Zanoni, Photoelectrocatalytic/photoelectro-Fenton coupling system using a nanostructured photoanode for the oxidation of a textile dye: kinetics study and oxidation pathway, Chemosphere 136 (2015) 63-71.

[22] Y. Nosaka, A. Nosaka, Understanding hydroxyl radical ($^{\bullet}$OH) generation processes in photocatalysis, ACS Energy Lett. 1 (2016) 356-359.

[23] E. Brillas, I. Sirés, M.A. Oturan, Electro-Fenton process and related electrochemical technologies based on Fenton's reaction chemistry, Chem. Rev. 109 (2009) 6570-6631.

[24] C.A. Martínez-Huitle, M.A. Rodrigo, I. Sirés, O. Scialdone, Single and coupled electrochemical processes and reactors for the abatement of organic water pollutants: a critical review, Chem. Rev. 115 (2015) 13362-13407.

[25] I. Sirés, E. Brillas, Remediation of water pollution caused by pharmaceutical residues based on electrochemical separation and degradation technologies: a review. Environ. Int. 40 (2012) 212-229.

[26] Y.B. Xie, X.Z. Li, Interactive oxidation of photoelectrocatalysis and electro-Fenton for azo dye degradation using TiO_2–Ti mesh and reticulated vitreous carbon electrodes, Mater. Chem. Phys. 95 (2006) 39-50.

[27] L.C. Almeida, B.F. Silva, M.V.B. Zanoni, Combined photoelectrocatalytic/electro-Fenton process using a Pt/TiO_2NTs photoanode for enhanced degradation of an azo dye: a mechanistic study, J. Electroanal. Chem. 734 (2014) 43-52.

[28] H. Zhang, X. Li, G. Chen, Fabrication of Photoelectrode Materials; in C. Comninellis, G. Chen (eds.), Electrochemistry for the Environment, Springer Science+Business Media, LLC, New York, USA, 2010.

[29] K.M. Beck, T. Sasaki, N. Koshizaki, Characterization of nanocomposite materials prepared via laser ablation of Pt/TiO_2 Bi-combinant targets, Chem. Phys. Lett. 301 (1999) 336-342.

[30] S. Murugesan, P. Kuppusami, N. Parvathavarthini, E. Mohandas, Pulsed laser deposition of anatase and rutile TiO_2 thin films, Surface Coat. Technol. 201 (2007) 7713-7719.

[31] M. Pelaez, N.T. Nolan, S.C. Pillai, M.K. Seery, P. Falaras, A.G. Kontos, P.S.M. Dunlop, J.W.J. Hamilton, J.A. Byrne, K. O'Shea, M.H. Entezari, D.D. Dionysiou, A review on the visible light active titanium dioxide photocatalysts for environmental applications, Appl. Catal. B: Environ. 125 (2012) 331-349.

[32] H.C. Arredondo Valdez, G. García Jiménez, S. Gutiérrez Granados, C. Ponce de León, Degradation of paracetamol by advance oxidation processes using modified reticulated vitreous carbon electrodes with TiO_2 and $CuO/TiO_2/Al_2O_3$, Chemosphere 89 (2012) 1195-1201.

[33] Ö. Kerkez, Í. Boz, Photo[electro)catalytic activity of Cu^{2+}-modified TiO_2 nanorod array thin films under visible light irradiation, J. Phys. Chem. Solids 75 (2014) 611-618.

[34] Z. Hua, Z. Dai, X. Bai, Z. Ye, P. Wang, H. Gu, X. Huang, Copper nanoparticles sensitized TiO_2 nanotube arrays electrode with enhanced photoelectrocatalytic activity for diclofenac degradation, Chem. Eng. J., 283 (2016) 514-523.

[35] H.M. Sung-Suh, J.R. Choi, H.J. Hah, S.M. Koo, Y.C. Bae, Comparison of Ag deposition effects on the photocatalytic activity of nanoparticulate TiO_2 under visible and UV light irradiation, J. Photochem. Photobiol. A: Chem. 163 (2004) 37-44.

[36] R.B. Domínguez-Espíndola, C. Bruguera-Casamada, S. Silva-Martínez, R.M. Araujo, E. Brillas, I. Sirés, Photoelectrocatalytic inactivation of *Pseudomonas aeruginosa* using an Ag-decorated TiO_2 photoanode, Separ. Purif. Technol. 208 (2019) 83-91.

[37] Z. Zhang, Y. Yu, P. Wang, Hierarchical top-porous/bottom-tubular TiO_2 nanostructures decorated with Pd nanoparticles for efficient photoelectrocatalytic decomposition of synergistic pollutants, ACS Appl. Mater. Interfaces 4 (2012) 990-996.

[38] A. Pandikumar, S. Murugesan, R. Ramaraj, Functionalized silicate sol-gel-supported TiO_2-Au core-shell nanomaterials and their photoelectrocatalytic activity, ACS Appl. Mater. Interfaces 2 (2010) 1912-1917.

[39] Wang, H.; You, T.; Shi, W.; Li, J.; Guo, L. Au/TiO_2/Au as a plasmonic coupling photocatalyst. J. Phys. Chem. C 116 (2012) 6490-6494.

[40] A. Ayati, A. Ahmadpour, F.F. Bamoharram, B. Tanhaei, M. Mänttäri, M. Sillanpää, Review on catalytic applications of Au/TiO_2 nanoparticles in the removal of water pollutant, Chemosphere 107 (2014) 163-174.

[41] K.H.W. Ho, A. Shang, F. Shi, T.W. Lo, P.H. Yeung, Y.S. Yu, X. Zhang, K.-L. Wong, D.Y. Lei, Plasmonic Au/TiO_2-dumbbell-on-film nanocavities for high-efficiency hot-carrier generation and extraction, Adv. Funct. Mater. (2018) 1800383.

[42] E. György, G. Sauthier, A. Figueras, A. Giannoudakos, M. Kompitsas, I.N. Mihailescu, Growth of Au–TiO_2 nanocomposite thin films by a dual-laser, dual-target system, J. Appl. Phys. 100 (2006) 114302.

[43] G. Sahu, K. Wang, S.W. Gordon, W. Zhou, M.A. Tarr, Core-shell Au–TiO_2 nanoarchitectures formed by pulsed laser deposition for enhanced efficiency in dye sensitized solar cells, RSC Adv. 2 (2012) 3791-3800.

[44] A. Maizelis, Multilayer nickel–copper anode for direct glucose fuel cell, J. Electrochem. En. Conv. Stor. 16 (2019) 041003.

[45] A. Maizelis, B. Bairachny, Voltammetric analysis of phase composition of Zn-Ni alloy thin films electrodeposited from weak alkaline polyligand electrolyte, J. Nano-Electron. Phys. 9 (2017) 05010.

[46] UNESCO, Emerging Pollutants in Water Series, Vol. 1, Pharmaceuticals in the Aquatic Environment of the Baltic Sea Region – A Status Report; 2017.

[47] Becker’s Hospital Review; https://www.beckershospitalreview.com/supply-chain/10-most-popular-prescription-drugs-for-2017.html (last access in 2017).

[48] E. Brillas, I. Sirés, Electrochemical removal of pharmaceuticals from water streams: reactivity elucidation by mass spectrometry, TrAC-Trend. Anal. Chem. 70 (2015) 112-121.

[49] L. Liu, R. Li, Y. Liu, J. Zhang, Simultaneous degradation of ofloxacin and recovery of Cu(II) by photoelectrocatalysis with highly ordered TiO_2 nanotubes, J. Hazard. Mater. 308 (2016) 264-275.

[50] I. Tantis, L.G. Bousiakou, P. Lianos, H. Kalkan, A study of the photocatalytic and photoelectrocatalytic degradation of diclofenac sodium using nanocrystalline TiO_2 films, J. Mater. Environ. Sci. 8 (2017) 1-6.

[51] P. Mazierski, A. Fiszka, P. Wilczewska, A. Białk-Bielińska, A. Zaleska-Medynska, E. Siedlecka, Removal of 5-fluorouracil by solar-driven photoelectrocatalytic oxidation using Ti/TiO_2(NT) photoelectrodes, Water Res. 157 (2019) 610-620.

[52] Y. Cui, Q. Meng, X. Deng, Q. Ma, H. Zhang, X. Cheng, X. Li, M. Xie, Q. Cheng, Fabrication of platinum nano-crystallites decorated TiO_2 nano-tube array photoelectrode and its enhanced photoelectrocatlytic performance for degradation of aspirin and mechanism, J. Ind. Eng. Chem. 43 (2016) 177-184.

[53] D. Li, J. Jia, T. Zheng, X. Cheng, X. Yu, Construction and characterization of visible light active Pd nano-crystallite decorated and C-N-S-co-doped TiO_2 nanosheet array photoelectrode for enhanced photocatalytic degradation of acetylsalicylic acid, Appl. Catal. B: Environ. 188 (2016) 259-271.

[54] R. Burgos-Castillo, M. Sillanpää, E. Brillas, I. Sirés, Removal of metals and phosphorus recovery from urban anaerobically digested sludge by electro-Fenton treatment, Sci. Total Environ. 644 (2018) 173-182.

[55] E. Bocos, E. Brillas, M.A. Sanromán, I. Sirés, Electrocoagulation: simply a phase separation technology? The case of bronopol compared to its treatment by EAOPs, Environ. Sci. Technol. 50 (2016) 7679-7686.

[56] Z. Jiang, W. Zhang, L. Jin, X. Yang, F. Xu, J. Zhu, W. Huang, Direct XPS evidence for charge transfer from a reduced rutile $TiO_2(110)$ surface to Au clusters, J. Phys. Chem. C 111 (2007) 12434-12439.

[57] Y. Wu, J. Zhang, L. Xiao, F. Chen, Preparation and characterization of TiO_2 photocatalysts by Fe^{3+} doping together with Au deposition for the degradation of organic pollutants, Appl. Catal. B: Environ. 88 (2009) 525-532.

[58] N. Kruse, S. Chenakin, XPS Characterization of Au/TiO_2 catalysts: binding energy assessment and irradiation effects, Appl. Catal. A: Gen. 391 (2011) 367-376.

[59] V. Madhavi, P. Kondaiah, G. Mohan Rao, influence of silver nanoparticles on titanium oxide and nitrogen doped titanium oxide thin films for sun light photocatalysis, Appl. Surf. Sci. 436 (2018) 708-719.

[60] D. Sánchez-Rodríguez, M.G.M. Medrano, H. Remita, V. Escobar-Barrios, Photocatalytic properties of $BiOCl-TiO_2$ composites for phenol photodegradation, J. Environ. Chem. Eng. 6 (2018) 1601-1612.

[61] Y.-F. Zhu, J. Zhang, L. Xu, Y. Guo, X.-P. Wang, R.-G. Du, C.-J. Lin, Fabrication and photoelectrochemical properties of $ZnS/Au/TiO_2$ nanotube array films, Phys. Chem. Chem. Phys. 15 (2013) 4041-4048.

[59] Q. Sun, Y.-P. Peng, H. Chen, K.-L. Chang, Y.-N. Qiu, S.-W. Lai, Photoelectrochemical oxidation of ibuprofen via Cu_2O-doped TiO_2 nanotube arrays, J. Hazard. Mater. 319 (2016) 121-129.

[63] J. Tian, H. Gao, H. Kong, P. Yang, W. Zhang, J. Chu, Influence of transition metal doping on the structural, optical, and magnetic properties of TiO_2 films deposited on Si substrates by a sol–gel process, Nanoscale Res. Lett. 8 (2013) 533.

[64] J. Singh, K. Sahu, A. Pandey, M. Kumar, T. Ghosh, B. Satpati, T. Som, S. Varma, D.K. Avasthi, S. Mohapatra, Atom beam sputtered Ag-TiO_2 plasmonic nanocomposite thin films for photocatalytic applications, Appl. Surf. Sci. 411 (2017) 347-354.

[65] Y. Zhang, C.X. Harris, P. Wallenmeyer, J. Murowchick, X. Chen, Asymmetric lattice vibrational characteristics of rutile TiO_2 as revealed by laser power dependent Raman spectroscopy. J. Phys. Chem. C 117 (2013) 24015-24022.

[66] K. Drogowska, Z. Tarnawski, A. Brudnik, E. Kusior, M. Sokołowski, K. Zakrzewska, A. Reszka, N.T.H. Kim-Ngan, A.G. Balogh, RBS, XRR and optical reflectivity measurements of Ti–TiO_2 thin films deposited by magnetron sputtering, Mater. Res. Bull. 47 (2012) 296-301.

[67] E. Arcadipane, R. Sanz, M. Miritello, G. Impellizzeri, M.G. Grimaldi, V. Privitera, L. Romano, TiO_2 Nanowires on Ti thin film for water purification, Mater. Sci. Semicond. Process. 2016, 42 (2016) 24-27.

[68] E. Alves, N. Franco, N.P. Barradas, B. Nunes, J. Lopes, A. Cavaleiro, M. Torrell, L. Cunha, F. Vaz, Structural and optical studies of Au doped titanium oxide films, Nucl. Instr. Meth. Phys. Res. B: Beam Interact. Mater. Atoms 272 (2012) 61-65.

[69] A.M. Goodman, Optical interference method for the approximate determination of refractive index and thickness of a transparent layer, Appl. Opt. 17 (1978), 2779-2787.

[70] J. Tauc, Optical Properties and Electronic Structure of Amorphous Semiconductors, in: S. Mitra, (ed.), Optical Properties of Solid, Papers from the NATO Advanced Study Institute on Optical Properties of Solids held August 7–20, 1966, at Freiburg, Germany, Springer, Boston, USA, 1969.

[71] T.E. Tiwald, M. Schubert, Measurement of rutile TiO_2 dielectric tensor from 0.148 to 33 μm using generalized ellipsometry, Proceedings of SPIE - The International Society for Optical Engineering 4103 (2000) 19-29.

[72] A. Wahl, K. Dawson, N. Sassiat, A.J. Quinn, A. O'Riordan, Nanomolar trace metal analysis of copper at gold microband arrays, J. Phys. Conf. Ser. 307 (2011) 01206.

[73] D. Li, X. Guo, H. Song, T. Sun, J. Wan, Preparation of RuO_2-TiO_2/nano-graphite composite anode for electrochemical degradation of ceftriaxone sodium, J. Hazard. Mater. 351 (2018) 250-259.

[74] M.V.B. Zanoni, J.J. Sene, H. Selcuk, M.A. Anderson, Photoelectrocatalytic production of active chlorine on nanocrystalline titanium dioxide thin-film electrodes, Environ. Sci. Technol. 38 (2004) 3203-3208.

[75] I. Sirés, J.A. Garrido, R.M. Rodríguez, P.L. Cabot, F. Centellas, C. Arias, E. Brillas, Electrochemical degradation of paracetamol from water by catalytic action of Fe^{2+}, Cu^{2+}, and UVA light on electrogenerated hydrogen peroxide, J. Electrochem. Soc. 153 (2006) D1-D9.

[76] E. Brillas, I. Sirés, C. Arias, P.L. Cabot, F. Centellas, R.M. Rodríguez, J.A. Garrido, Mineralization of paracetamol in aqueous medium by anodic oxidation with a boron-doped diamond electrode, Chemosphere 58 (2005) 399-406.

[77] L.C. Almeida, S. Garcia-Segura, N. Bocchi, E. Brillas, Solar photoelectro-Fenton degradation of paracetamol using a flow plant with a Pt/air-diffusion cell coupled with a compound parabolic collector: Process optimization by response surface methodology, Appl. Catal. B: Environ. 103 (2011) 21-30.

Figure captions

Fig. 1. General XPS spectrum of the $TiO_2/Au/TiO_2$ multilayer thin film.

Fig. 2. Raman spectrum of the $TiO_2/Au/TiO_2$ multilayer thin film.

Fig. 3. EFA characterization of (A) $TiO_2/Au/TiO_2$ multilayer thin film, (B) Ti^{4+}, and (C) Au.

Fig. 4. (A) Transmittance spectrum of the TiO_2 thin film and $TiO_2/Au/TiO_2$ multilayer thin film. (B) Tauc plot for the determination of the band gap of the undoped and doped films.

Fig. 5. (A) Qualitative comparison of the photoluminescence emission spectra of the $TiO_2/Au/TiO_2$ film (blue curve) and a TiO_2 blank (red curve) from 3.6 to 2.0 eV. (B) Detailed photoluminescence emission spectrum of the same $TiO_2/Au/TiO_2$ multilayer thin film.

Fig. 6. Cyclic voltammograms of (A) pure gold, (B) undoped TiO_2 thin film, and (C) $TiO_2/Au/TiO_2$ multilayer thin film, all of 1 cm^2 geometric area, in 0.050 M N_2SO_4 at pH 3.0. The cell contained a Pt cathode and Ag|AgCl (3 M KCl) as reference electrode. Scan rate 100 mV s^{-1}.

Fig. 7. Normalized paracetamol concentration decay vs. electrolysis time for the (A) EO in 0.050 M Na_2SO_4, (B) PEC in 0.050 M Na_2SO_4, and (C) PEC in 0.035 M Na_2SO_4 + 0.015 M NaCl treatments of 100 mL of solutions with different drug concentrations at pH 3.0 using a three-electrode cell with a $TiO_2/Au/TiO_2$ multilayer thin-film anode and a stainless steel cathode at I_{app} = 0.50 mA. The PEC trials were performed with irradiation from a 36-W LED UVA lamp.

Fig. 8. Change of normalized paracetamol concentration with electrolysis time for the PEC + PEF treatment of 100 mL of 39 mg L^{-1} of drug in 0.035 M Na_2SO_4 + 0.015 M NaCl and 0.50 mM Fe^{2+} at pH 3.0 using a three-electrode cell containing a $TiO_2/Au/TiO_2$ multilayer thin-film anode and an air-diffusion cathode, at E_{an} = +4.0 V vs Ag|AgCl (3 M KCl), with irradiation from a 36-W LED UVA lamp.

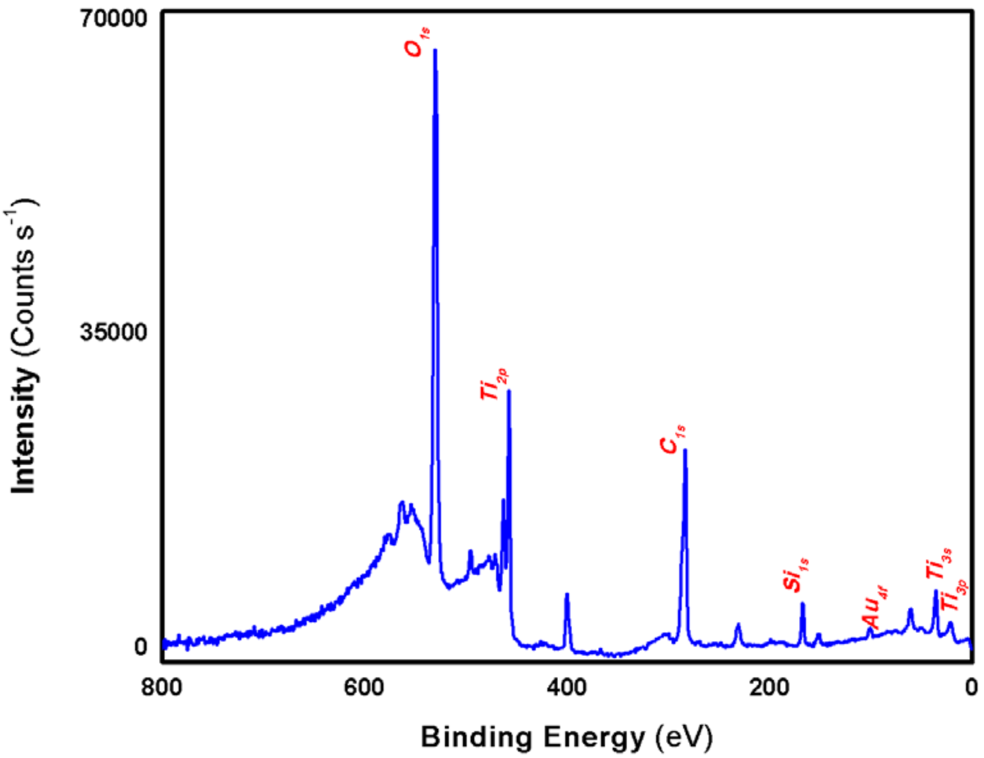
70000
35000
0
Intensity (Counts s^{-1})
O_{1s}
Ti_{2p}
C_{1s}
Si_{1s}
Au_{4f}
Ti_{3s}
Ti_{3p}
800
600
400
200
0
Binding Energy (eV)

Fig. 1

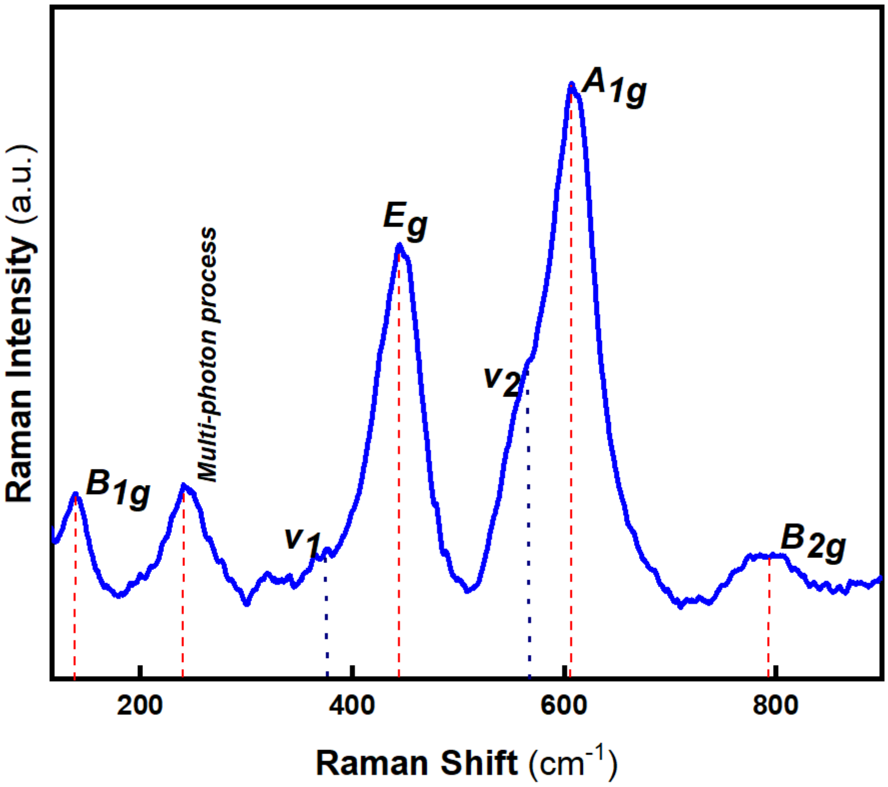
Raman Intensity (a.u.)
Raman Shift (cm^{-1})
200
400
600
800
B_{1g}
Multi-photon process
v_1
E_g
v_2
A_{1g}
B_{2g}

Fig. 2

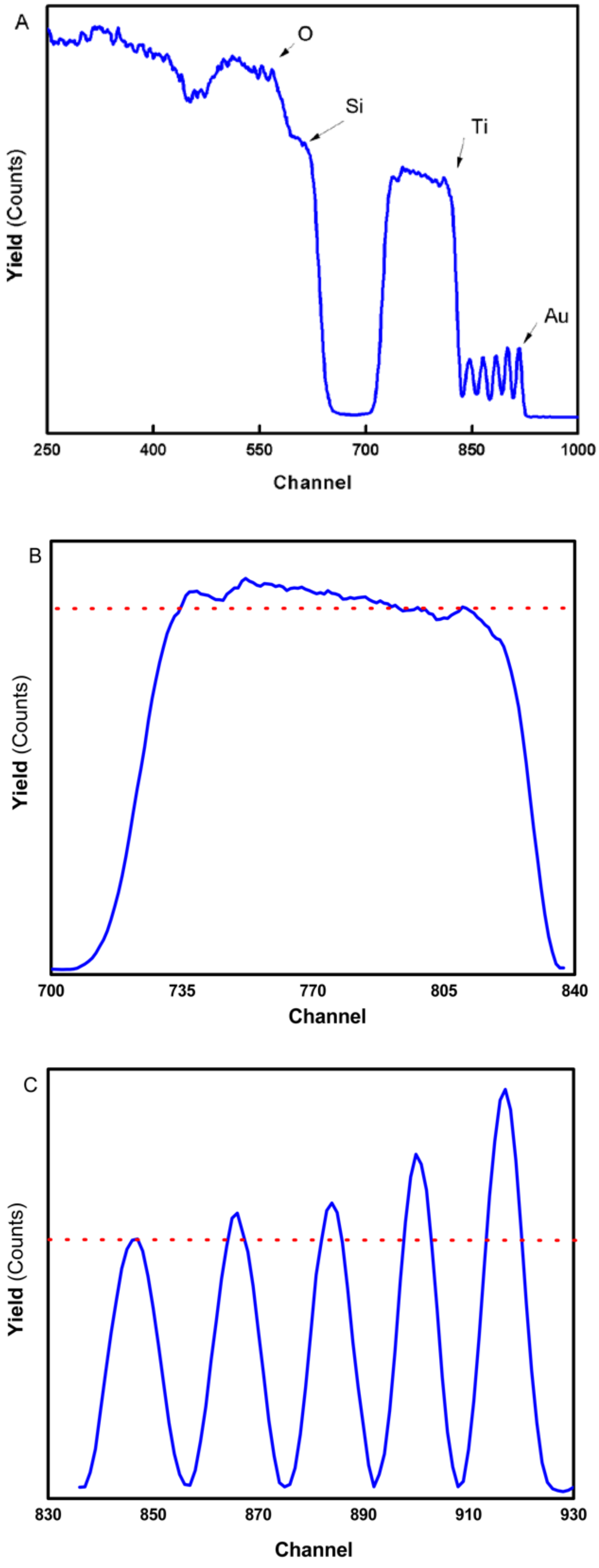
A
O
Si
Ti
Au
Yield (Counts)
250
400
550
700
850
1000
Channel
B
Yield (Counts)
700
735
770
805
840
Channel
C
Yield (Counts)
830
850
870
890
910
930
Channel

Fig. 3

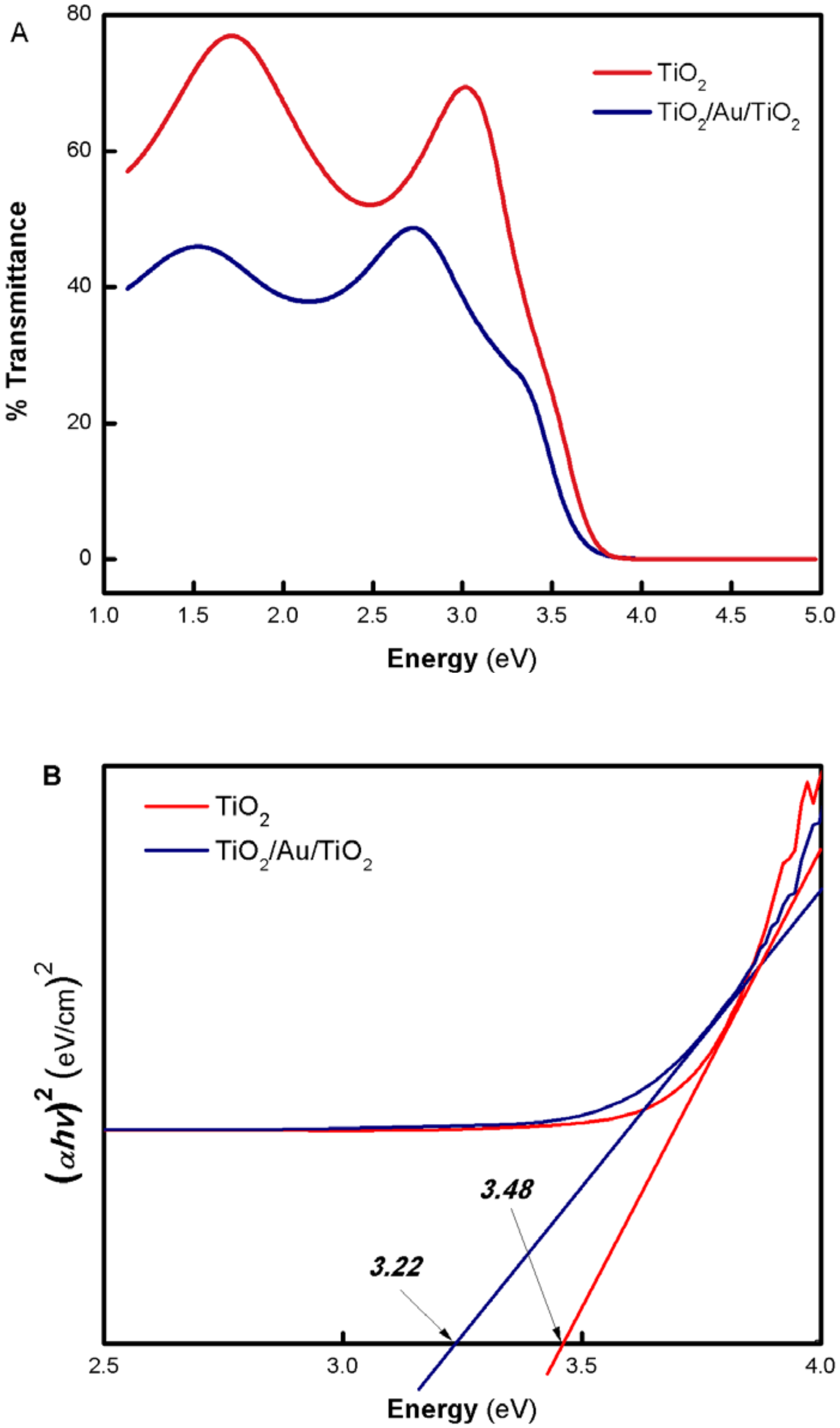
A
80
60
40
20
0
% Transmittance
TiO_2
$TiO_2/Au/TiO_2$
1.0
1.5
2.0
2.5
3.0
3.5
4.0
4.5
5.0
Energy (eV)
B
TiO_2
$TiO_2/Au/TiO_2$
$(\alpha h\nu)^2$ (eV/cm)^2
3.48
3.22
2.5
3.0
3.5
4.0
Energy (eV)

Fig. 4

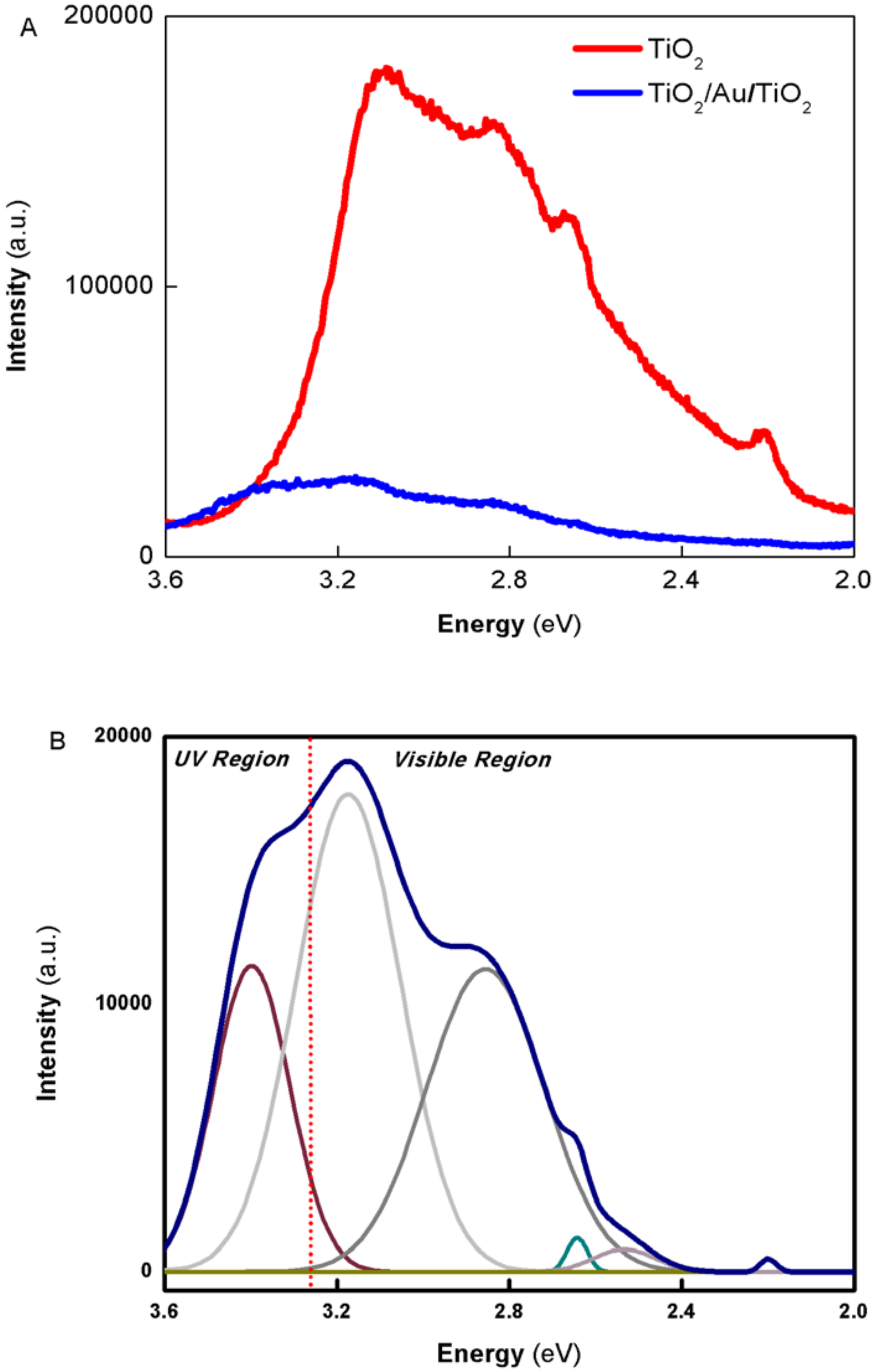
A
200000
100000
0
Intensity (a.u.)
TiO$_2$
TiO$_2$/Au/TiO$_2$
3.6
3.2
2.8
2.4
2.0
Energy (eV)
B
20000
10000
0
Intensity (a.u.)
UV Region
Visible Region
3.6
3.2
2.8
2.4
2.0
Energy (eV)

Fig. 5

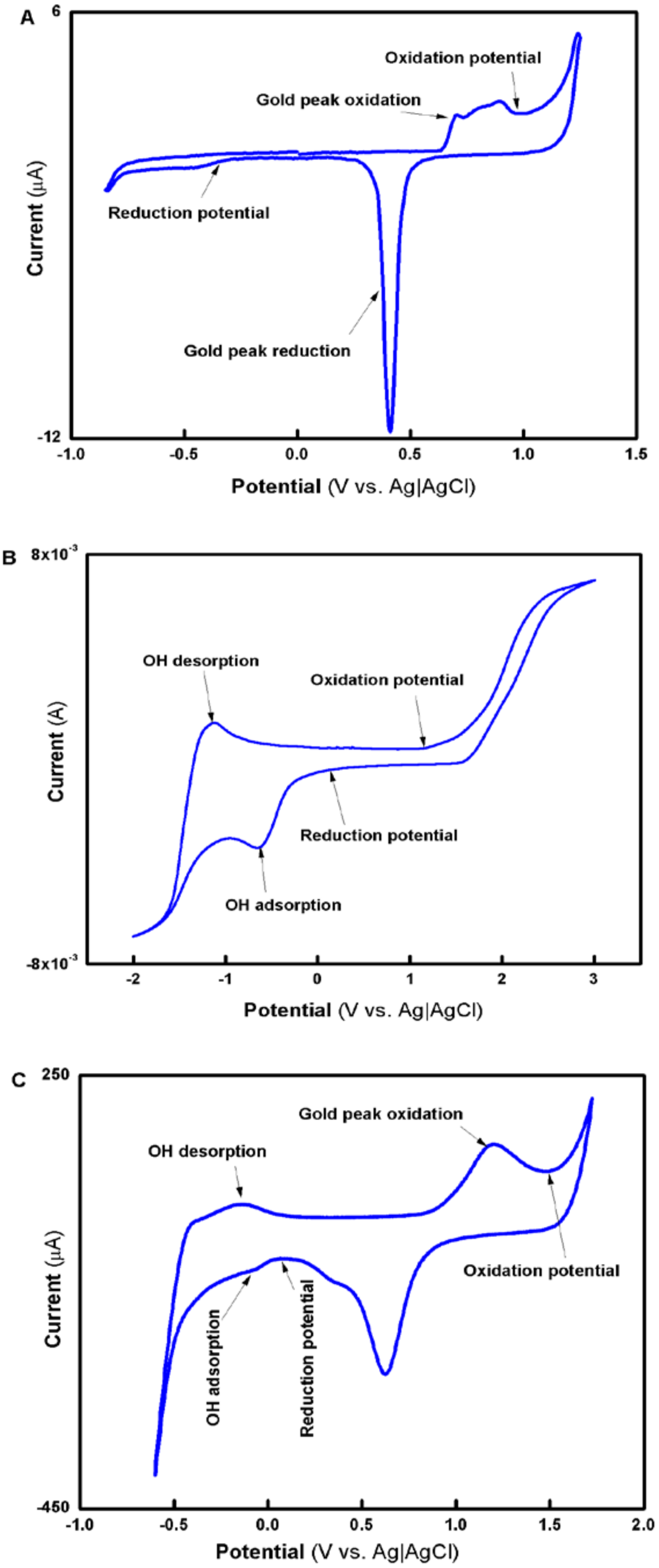
A
6
-12
Current (μA)
Oxidation potential
Gold peak oxidation
Reduction potential
Gold peak reduction
-1.0
-0.5
0.0
0.5
1.0
1.5
Potential (V vs. Ag|AgCl)
B
8x10^{-3}
-8x10^{-3}
Current (A)
OH desorption
Oxidation potential
Reduction potential
OH adsorption
-2
-1
0
1
2
3
Potential (V vs. Ag|AgCl)
C
250
-450
Current (μA)
Gold peak oxidation
OH desorption
Oxidation potential
OH adsorption
Reduction potential
-1.0
-0.5
0.0
0.5
1.0
1.5
2.0
Potential (V vs. Ag|AgCl)

Fig. 6

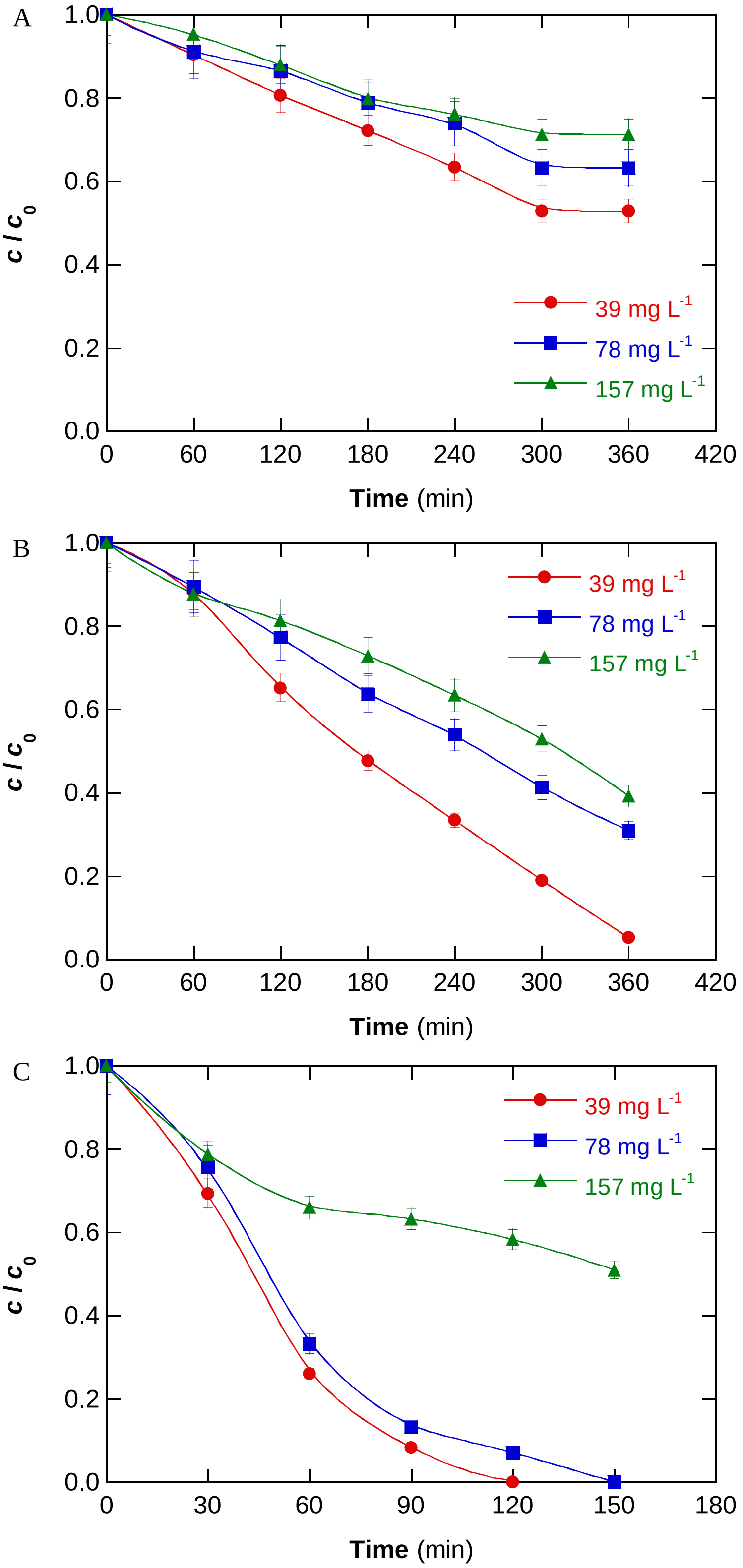
A
B
C
1.0
0.8
0.6
0.4
0.2
0.0
c / c0
0
60
120
180
240
300
360
420
30
90
150
Time (min)
39 mg L-1
78 mg L-1
157 mg L-1

Fig. 7

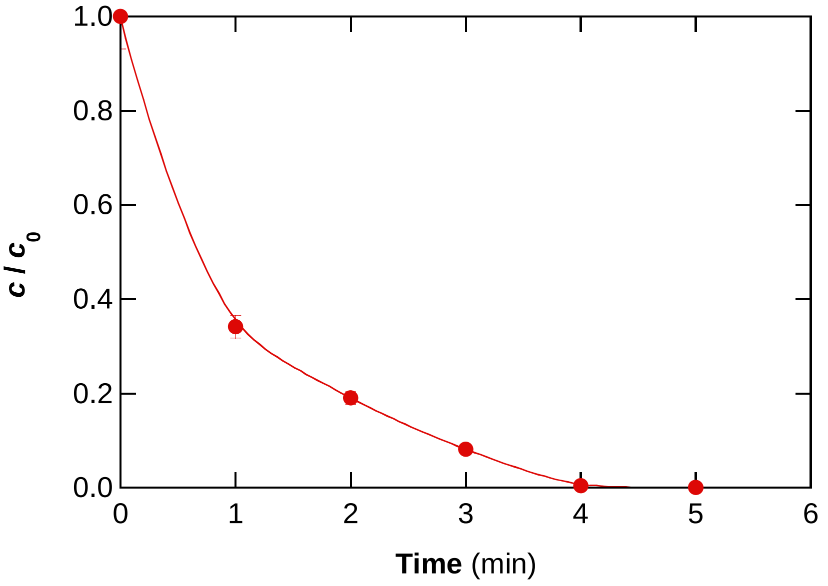

Fig. 8